Microfluidic control of nucleation and growth of $CaCO_3$

Lei Li, Jesus Rodriguez Sanchez, Felix Kohler, Anja Røyne, and Dag Kristian Dysthe*

Physics of Geological Processes (PGP), The NJORD Centre, Department of Physics, University of Oslo, POBox 1048 Blindern, 0316 Oslo

E-mail: d.k.dysthe@fys.uio.no
Phone: +47 90940996

Abstract

A novel method for studying nucleation and growth of $CaCO_3$ crystals in situ has been developed and tested rigorously. We demonstrate that precise flow control is essential and how this is achieved. The method has the advantage that one may study single crystals of polymorphs that are thermodynamically unstable in collections of many crystals and that one obtains precise and accurate growth rates without any extra assumptions. We also demonstrate that at low supersaturations where 2D nucleation does not occur we measure the growth rate constant of calcite to be 5 times larger than that reported by batch methods and two orders of magnitude larger than measured by AFM. Considering the large interest in calcite growth in for example geoscience, environmental science, and industry we consider that it is important to explain the discrepancy of growth rate constants between different methods. The method presented here can easily be applied to many other minerals.

Introduction

Calcium carbonate ($CaCO_3$) makes up about 4% of the Earth's crust, it is the major long term sink in the global carbon dioxide cycle,[1–3] 60% of the worlds oil is held in carbonate reservoirs[4] and it is probably the most studied biomineral.[5–7] Industrially it is used in paper, plastics, paints, coatings, personal health, food production, building materials and construction.[8] The modelling of biomineralization, geological, industrial and climate processes involving calcium carbonate relies on firm knowledge of $CaCO_3$ crystal growth mechanisms and rates.[9,10] Much effort has therefore been invested in such fundamental studies.[11–17] Although nanoscale measurements have revealed the fundamental mechanisms of growth, the rates measured by atomic force microscopy (AFM)[9,16] do not agree well with macroscopic methods.[11] The purpose of this study is to develop a new technique at an intermediate scale to study the nucleation and growth of whole crystals. This allows direct measurement of surface normal growth rate and dispels the need for additional measurements or assumptions.

Since the first *in situ* AFM studies of calcite dissolution and growth[12] the AFM has been invaluable in building our understanding of the calcite surface.[17] *In situ* AFM observations allow the determination of step growth velocities of small portions of a surface (preferably a well-defined screw dislocation[16]). AFM studies of calcite growth[12–17] give detailed input for microkinetic modelling,[10,18] but upscaling relies on knowledge of dislocation density[16] or step densities.[9] AFM studies see only single screw dislocations and not ensembles of them on entire crystal surfaces.

Batch experiments measure (and sometimes control) fluid supersaturation during growth of a large number of calcite grains that are present as crystallization seeds.[11,19] The calculation of crystal growth rate from such experiments is highly dependent on the estimation of reactive surface area of the seed crystals. Batch measurements have the advantage of measuring average rates over thousands of surfaces but cannot observe the mechanisms of crystal growth.

Calcite *dissolution* rates measured by different methods show large variation.[20–22] In order to bridge the gap in information and scales of AFM measurements and batch measurements for calcite *dissolution*, whole crystal studies have been performed by interferometry ex situ[20] and in situ.[23] These *dissolution* studies of whole crystals do not rely on extra parameters like dislocation density or reactive surface area We claim that more whole crystal studies of $CaCO_3$ *growth* under well controlled conditions are also necessary and present here a novel microfluidic and microscopy method to fill the gap in length scales.

Microfluidics and $CaCO_3$

Compared to batch methods and AFM, microfluidics represents a relatively young but promising platform to run nucleation and growth experiments due to its high level of control over diffusion, concentration, flow dynamics, water-oil interface, liquid-gas interface and other factors to the degree that bulk methods can hardly reach.

Most microfluidic studies dealing with $CaCO_3$ focus on nucleation and early growth of different $CaCO_3$ polymorphs. Some study hydrophobicity of $CaCO_3$ coatings,[24,25] use $CaCO_3$ as source for Ca ions to produce alginate hydrogels or capsules[26–30] or to form hollow $CaCO_3$ nanoparticles for drug delivery.[31] Other studies of dissolution,[23] reactive flow[32–34] and calcite wetting of single or multiphase flow[35,36] have also been performed in microfluidic networks.

Studies in nucleation and growth of $CaCO_3$ polymorphs in microfluidics are mainly intended to cast light on fundamental aspects of inorganic $CaCO_3$ crystallization pathways[37–39] or biomimetic or biomineralization processes.[40–49]

Zeng et al[39] used microfluidics to control the formation of ACC and transformation pathways to vaterite and calcite, Li et al[38] also studied crystallization pathways but included the use of FTIR in microfluidics and Rodriguez-Ruiz[37] studied how confinement in microfluidic reactors stabilized the hydrated $CaCO_3$ mineral ikaite. Yashina et al[45] used ex situ SEM to study nucleation and initial growth of $CaCO_3$ polymorphs formed by mixing Na_2CO_3 and $CaCl_2$ in microfluidic droplets, Gong et al,[47] used a gas-liquid microfluidic system to study growth of calcite crystals around obstacles and Kim et al[49] used a similar system to study early stages of $CaCO_3$ growth in presence of additives. Seo et al[46] mixed Na_2CO_3 and $CaCl_2$ in a microfluidic linear gradient mixer to study $CaCO_3$ crystallization morphologies. In another set of studies[40,43,44] they mixed Na_2CO_3 and $CaCl_2$ with and without mollusk shell proteins in a microfluidic T-junction to study $CaCO_3$ crystallization polymorphs. A similar T-junction and fluids were employed to study $CaCO_3$ polymorphs in situ by synchrotron X-ray methods.[48] Neira-Carrillo[41,42] studied templated $CaCO_3$ growth on different polymers.

$CaCO_3$ nucleation studies usually involve segmented-flow mixing of reagents, i.e., nucleation occurs within droplets, while very few operate under continuous-flow conditions. The novelty of the present study is the use of a microfluidic continuous flow reactor to induce nucleation and slow growth of $CaCO_3$ crystals from the surrounding solution under highly controlled conditions. This also enables the study of thermodynamically unstable polymorphs.

Experimental

The aim of the experimental setup is to nucleate calcium carbonate crystals in a limited area that allows: i) high resolution imaging access, ii) controlling which polymorph to keep in the system for study, iii) controlling the saturation conditions at the growing crystal surface, iv) allowing slow growth of crystals from the nu-

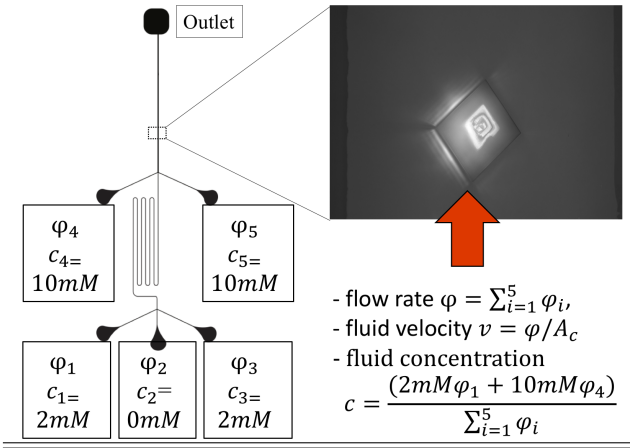

	φ_1 $\frac{\mu l}{min}$	φ_2 $\frac{\mu l}{min}$	φ_3 $\frac{\mu l}{min}$	φ_4 $\frac{\mu l}{min}$	φ_5 $\frac{\mu l}{min}$	φ $\frac{\mu l}{min}$	u $\frac{mm}{s}$	c mM
Nucl.	1	0.5	1	2	2	6.5	20	3.4
Growth	1	0.5	1	0	0	2.5	7.7	0.8
Sat.	1	2	1	0	0	4	12	0.5

Figure 1: *Flow rate control for nucleation and growth. The fluid concentration in the channel at the crystal depends on the relative flow rates of the 5 inlets. $CaCl_2$ is injected through inlets 1 and 4 and Na_2CO_3 is injected through inlets 3 and 5. Inlets 4 and 5 are only used during nucleation to assure nucleation in the channel between the second junction and the outlet. During growth the concentration is varied by changing φ_2 in the range shown in the table.*

clei, v) measuring growth rates, and vi) avoiding clogging of the microfluidic device due to crystal growth elsewhere in the system.

Microfluidic devices

Two different microfluidic patterns were designed for this study. Figure 1 shows the pattern used for crystal nucleation and growth experiments where the channel dimensions are 120±2 μm wide and 45 μm high, the length from first to second junction is l_c=50 mm and the length from the second junction to the outlet is 10 mm. Figure 2 shows the pattern used for flow stability experiments where the channel dimensions are 70±2 μm wide and 45 μm high and the length from the junction to outlet is 20 mm.

The channel networks were designed in Adobe Illustrator, saved as pdf and used to print the photomask on a film substrate (Selba S.A, www.selba.ch). A photoresist (SU-8 GM1070, Gersteltec, www.gersteltec.ch) was spun on silicon wafers at different speeds for different thicknesses, UV radiated (UV-KUB2, http://www.kloe.fr) and developed with PGMEA (www.sigmaaldrich.com) according to producers data sheet. Channel networks were cast in PDMS (Dow Corning Sylgard-184A, www.sigmaaldrich.com) with a 1:10 elastomer to curing agent ratio. Inlets and outlets of 1.5 mm diameter were punched subsequently and both the PDMS and glass covers were treated with corona plasma (Electro-Technic Model BD-20V, http://www.electrotechnicproducts.com) before assembly.

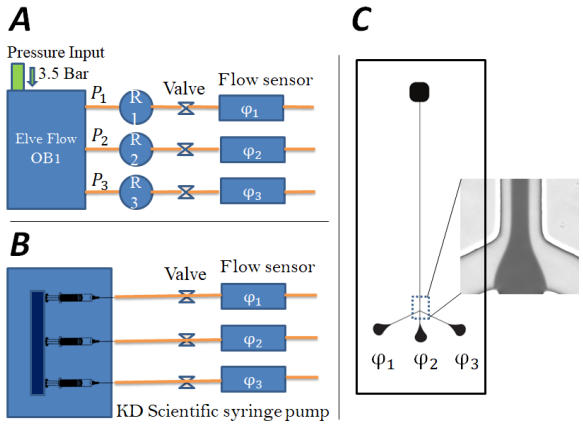

Figure 2: *Flow rate control for flow stability tests. The two system A and B were connected to the microfluidic channels with pure water in channels 1 and 3 and dyed water in channel 2. System A could operate in two feedback modes: pressure control or flow control. The syringe pump was run with either glass or plastic syringes. The inset image shows the junctions where the coloured and uncoloured flows meet. These images and recordings from the flow sensors were used as independent measurements of flow balance in the channel.*

Nucleation and growth of carbonate crystals

Pure water, $CaCl_2$ solution and Na_2CO_3 solution are injected through separate inlets to the microfluidic device. The solutions meet at the junctions and the solutions are mixed by diffusion transversal to the flow. The fluid concentration in the channel at the crystal depends on the relative flow rates, ϕ_i, at the 5 inlets

that have fixed solution concentrations (see Figure 1). Separate sections below will treat the difficulty of maintaining sufficiently good control of flow rates during the experiments. To ensure good mixing of the solution, the diffusion time scale for mixing, $\tau_D = (w/2)^2/D = 3$ s (where w=120 μm is the channel width and $D = 1.1 \cdot 10^{-9}$ m/s is the mean diffusion coefficient of the ions in water), is smaller than the time, $\tau_{mix} = l_c/u = 4 - 7$ s, it takes for the fluid to arrive at the growing crystal.

Nucleation of a crystal within the microfluidic channel was carried out in two steps. First, the channel was filled with deionized water at a flow rate $\varphi_1 = 0.5\mu$l/min from inlet 2. 2mM $CaCl_2$ and Na_2CO_3 solutions were subsequently injected at inlets 1 and 3 to achieve a $CaCO_3$ concentration of c=0.8 mM. This value was sufficiently low to avoid any nucleation. When the flow reached a stable behaviour, the 10mM $CaCl_2$ and Na_2CO_3 solutions, were injected into the channel from inlets 4 and 5 (using 2.5mL Halmiton 1000 syringes on a KD Scientific Legato 180 syringe pump) to achieve a $CaCO_3$ concentration of c =3.4 mM.

Once we observed crystals sticking to the glass or to the PDMS surface, the flows φ_4 and φ_5 were stopped. There is a certain probability that the first nucleus be either calcite, vaterite or aragonite, in our conditions the probability was roughly 50/50 calcite/vaterite in agreement with the measurements of Ogino et al.[50] In the remainder of the experiment we always chose to observe the crystal furthest upstream to be sure that the fluid concentration was determined by the flow rates and was not affected by other crystals upstream. Since the crystal is unaffected by other crystals and fully controlled by the concentration of the flowing solution we could dissolve and grow any $CaCO_3$ polymorph at will. Before calcite growth experiments we would dissolve vaterite at $c = 0.5$ mM while keeping the calcite crystal unchanged. We performed calcite growth rate experiments with concentrations in the range 0.55-0.8 mM.

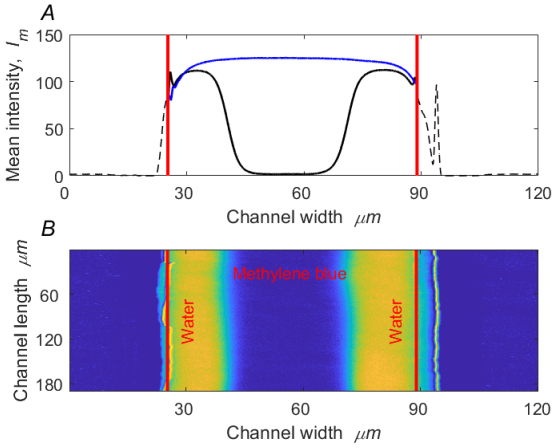

Figure 3: *Calculation of water and methylene-blue relative volume ratio from difference image.* **Bottom:** *The intensity difference between an image of water and methylene blue flowing in a part of the PDMS channel.* **Top:** *The mean intensities I_m along the width of the channel for water/methylene-blue/water solution (black line) and only water in the channel (blue line). The red vertical lines define the edge of the channel, x_1 and x_2. The black dashed line show the mean intensity outside the channel.*

Flow rate control

In our microfluidic experiments, the flow stability is extremely important to achieve the stable concentrations necessary for crystal growth. After struggling with many random nucleation and dissolution events in our first setup using syringe pumps we decided to test the stability of the flows. The stability of the syringe pump and gas pressure control systems are separately tested as shown in Figure 2. The gas pressure control system includes an Elveflow controller (Elveflow OB1 mk3, www.elveflow.com) which has both flow rate and pressure control modes, flow valves (Elveflow MUX) and flow sensors (0.4-7 μL/min, Elveflow). The input pressures P_i are controlled by the OB1. The three inlets have the same flow resistance so that the pressure control mode is achieved by setting the same inlet pressures $P_1 = P_2 = P_3$. In flow rate mode, OB1 adjusts the pressure to keep each flow rate constant. The syringe pump system includes a syringe pump (KD Scientific legato 180, www.kdscientific.com), BD plastic syringe (BD science, www.bd.com), Halmiton glass syringe (Halmiton 1000 syringe series, www.hamiltoncompany.com), flow valve (Elve-

flow MUX) and flow sensors (0.4-7 μL/min, Elveflow). The flow rate is controlled by the speed of the plunger and the inner diameter of the syringe. Because the accuracy of the syringe diameters of plastic and glass syringes differ, we test their stability separately.

Figure 2 displays the configurations used to test the flow stability: water was injected into the channel from inlets 1 and 3 with the flow rates φ_1 and φ_3 and methylene-blue solution (CAS Number: 61-73-4, Aldon Corp www.aldon-chem.com) was injected through inlet 2 at flow rate φ_2 which created two water/methylene-blue interfaces. Images of the flows (see Figures 2C and 3B) was followed for 5 hours. By averaging the intensity of the image along Y direction, we plotted the averaged intensity I_m along X direction (Figure 3A). The channel edges x_1 and x_2 and the interface of the water/methylene blue were clearly identified by thresholding (see red lines in Figure 3A). The relative volume of water in the channel γ was used to study the flow stability:

$$\gamma = \frac{\bar{I_m}}{\bar{I_w}} = \frac{\int_{x_1}^{x_2} I_m dx}{\int_{x_1}^{x_2} I_w dx}, \qquad (1)$$

where $\bar{I_m}$ is the average image intensity of the water/methylene-blue/water solution in the channel (Figure 3A black line). And $\bar{I_w}$ means the average image intensity when there is only water in the channel (Figure 3A blue line) and x_1 and x_2 are the edges of the channel (Figure 3A red lines).

For the crystal growth experiments the flow rates φ_1, φ_2, φ_3, are $CaCl_2$, water, Na_2CO_3 instead of water, methylene-blue, water. The same flow rate fraction,γ, is proportional to the $CaCO_3$ concentration, c:

$$c = \frac{(c'\varphi_1 + c'\varphi_3)/2}{\sum_i \varphi_i} = \frac{c'}{2}\frac{\bar{I_m}}{\bar{I_w}} = \frac{c'}{2}\gamma, \qquad (2)$$

where c' is the concentration of the $CaCl_2$ and Na_2CO_3 solutions and the stability of γ shows the stability of the final $CaCO_3$ concentration c during crystal growth.

Solution preparation, concentration and saturation calculations

Na_2CO_3 and $CaCl_2$ 10 mM stock solutions were prepared using a balance (Mettler AE260 Delta Range) and deionized water (Millipore Direct-Q 3UV) as solvent: 122.7 mg of Na_2CO_3 (VWR Ref.27767.364 Assay 99.0 100.5%) were dissolved in 115.6 mL water and 126.0 mg of $CaCl_2 2H_2O$ (VWR Ref.22322.364 Assay 97.0 103.0%) were dissolved in 85.7 mL water. Then, they were left to equilibrate with atmospheric CO_2 for 48 hours. Subsequently, 2 mM solutions were prepared by diluting the stock solutions with deionized water (2mL from the stock solution were mixed with 8mL of deionized water) prior to each experiment. After dilution, they were immediately entered into pressure flasks using air at pressures between 1 and 2.2 atmospheres (absolute pressure).

The saturation index, Σ has been calculated by PHREEQC.[51] The supersaturation is $\Omega = IAP/K_{sp}$ and the saturation index is

$$\Sigma = \frac{\Delta\mu}{kT} = \ln\left(\frac{a_{Ca^{2+}} a_{CO_3^{2-}}}{K_{sp}}\right) = \ln(\Omega) \qquad (3)$$

We have used the value of the solubility product $K_{sp} = 10^{-8.54}$ that Teng et al.[16] found to correspond to when spirals on the $10\bar{1}4$ surface stopped growing. They used slightly different fluids than in our study and a fixed pH of 8.5 whereas our solutions were not buffered and the pH varied. The lack of constraints on pH causes some inaccuracy of the calculation of saturation index. The calcite crystals in this study changed from growth to dissolution at a concentration of c_{sat}=0.5 mM. The calculated saturation index at this concentration is Σ=-0.11. We assume that the inaccuracy is mainly a shift of the saturation point and that the saturation index has the correct dependency on concentration.

An unintended side effect of using air as pressurizing gas for flow control was that it allowed CO_2 at higher pressures to exchange with the solution. The final supersaturation of the fluid is influenced by the amount of absorbed CO_2. The pressure corrected saturation index Σ_p of

the solutions is calculated for solutions in equilibrium with air at the actual pressure driving the flow. Since the exchange between CO_2 in the air and the solution takes time and the gas pressure changes during an experiment, the equilibrium CO_2 concentration in the fluid at the driving pressure is an upper bound.

Imaging

All experiments were monitored using an Olympus GX71 microscope with a green LED light source with a wavelength of 550 nm (from ThorLabs www.thorlabs.com). UPLanFLN 100x/1.30 and UPLanFI 40x/0.75p objectives with resolution d=260 nm and 450 nm (from Olympus www.olympus-lifescience.com). Images were recorded using a Pointgrey camera (Mono, Grasshopper3, GS3-U3-91S6M-C, www.ptgrey.com) with 3376 x 2704 resolution and saved as 8 bit TIFF files. For the high resolution objective there were 5 pixels per resolution diameter d. The analysis of the image sequences was carried out using in-house developed scripts in Matlab (www.mathworks.com) and ImageJ (imagej.nih.gov/ij/).

Determination of growth rate

Calcite is a trigonal-rhombohedral crystal and one $(10\bar{1}4)$ face is at rest and parallel with the glass surface (see Figure 4). We measure the imaged position of the four crystal $(10\bar{1}4)$ faces that are almost perpendicular to the glass surface neglecting the difference between the calcite surface normal and the projection along the imaging plane. The positions of the four faces are determined by averaging intensities along the direction parallel to the face and finding the minimum intensity. The averaging along the crystal faces allows determination of the crystal face position relative to earlier positions with a resolution of ± 1 pixel $= \pm 50$ nm. The growth rates are determined by linear fits to the position data as function of time and the reported precision of the growth rates are the standard deviations of these fits.

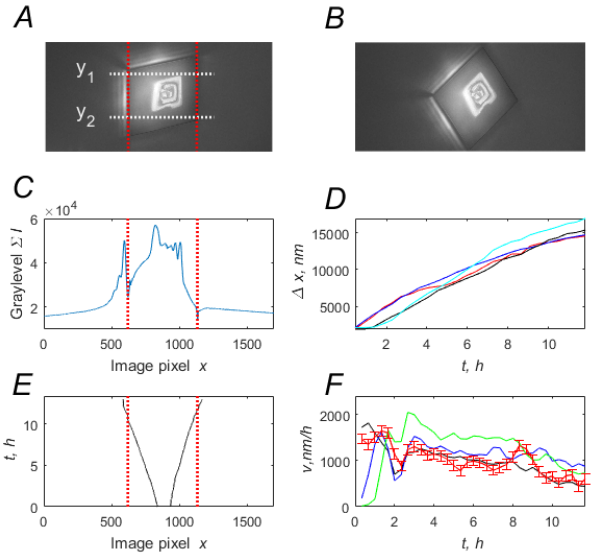

Figure 4: **Calculation of growth rates.** *Original image of crystal in* **B** *is rotated to have two faces vertical in* **A** *and the intensities between* y_1 *and* y_2 *are summed to produce the grey level plot in* **C**: $\sum_{i=1}^{2} I(y_i)$. *The local minima in the grey level identify the crystal face indicated by the red vertical lines. The minima positions in the images as function of time are displayed in* **E** *and the change in position,* Δx, *in* **D**. *Linear fits to* $\Delta x(t)$ *in smaller time windows yield the growth rates* v *in* **F**.

Results and discussion

Flow stability

The stability of the $CaCO_3$ concentration, c, which is proportional to the volume fraction in the flow (see equation (2)) is key to accurate and reliable measurements of crystal growth rates. The flow stability tests were performed for 5 hours with 2 water input channels at 1 μl/min and 1 input channel with dyed water at 2 μl/min and in four configurations: Gas pressure driven fluid flow with 1) pressure control (**PC**) and 2) flow control (**FC**) and syringe pump with 3) plastic syringe (**PS**) and 4) glass syringe (**GS**). The instantaneous volume fraction of dyed water presented in Figure 5 was calculated from images according to equation (2) and from the flow sensors.

In Figure 5 one observes that the flow control by syringe pump causes both constant deviation from the desired flow fraction, $\gamma = 0.5$, slow drift and large, sudden changes compared to the gas pressure driven flows. The constant deviation and slow drift are probably caused

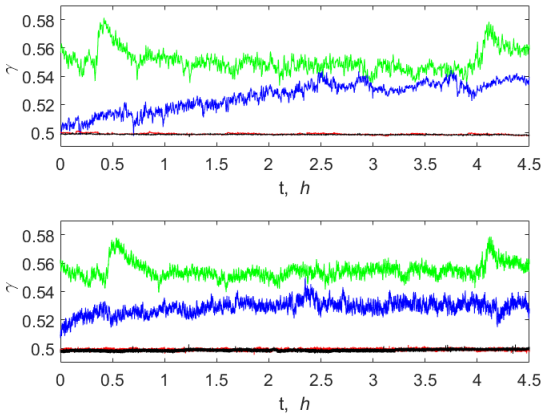

	$100 \cdot \sigma_\gamma/\bar{\gamma}$		$100 \cdot \Delta_\gamma/\bar{\gamma}$	
	Image	FS	Image	FS
GS	1.4	1.0	8.8	7.1
PS	2.0	0.9	9.0	8.1
FC	0.1	0.1	0.8	1.4
PC	0.1	0.1	0.7	1.3

Figure 5: *Stability of water/dyed water/water flow. The relative volume γ of dyed water calculated from images (top) and flow sensors (bottom) is displayed in* **black:** *pressure control (***PC***),* **red:** *flow control (***FC***),* **green:** *plastic syringe (***PS***) and* **blue:** *glass syringe (***GS***). Table: the relative standard deviation $\sigma_\gamma/\bar{\gamma}$ and the relative maximum deviation $\Delta_\gamma/\bar{\gamma}$ of the four flow stability tests.*

by differences in inner diameter of the syringes or by mechanical inaccuracies of the syringe pump. The short term fluctuations are probably caused by stick slip of the drive train in the pump or/and by the plunger in the syringe. We have also characterized the flow stability by the relative standard deviation of γ, $\sigma_\gamma/\bar{\gamma}$ and the relative difference between the maximum and minimum value, $\Delta_\gamma/\bar{\gamma}$ (where $\bar{\gamma}$ is the average of γ) displayed in Figure 5. These measures demonstrate that the fluctuations in flow fraction (and thereby concentration) is one order of magnitude larger for the syringe pump. The relative maximum deviation, $\Delta_\gamma/\bar{\gamma}$, captures rare events of high and low concentrations and is related to the probability of uncontrolled nucleation events during the crystal growth. The large fluctuations for the syringe pump explains our problems of sudden nucleation events and ruined experiments while using syringe pumps. The gas pressure flow control system on the other hand provides a stable

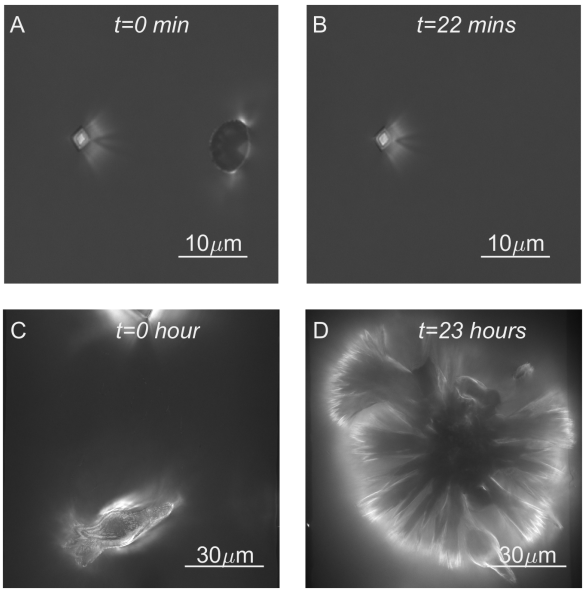

Figure 6: **Top (A and B):** *A. Calcite and Vaterite nuclei at the same time and attached at the middle of the channel. B. The vaterite disappeared after 22 minutes flushing with 0.5mM $CaCO_3$ solution.* **Bottom C.D:** *C. A aragonite located in the channel. D. The aragonite grows to fill the channel after 7 hours growth at 0.8 mM $CaCO_3$ concentration. The radius of aragonite crystal increase at a rate of 4160 nm/h.*

concentration during all our many hours long experiments with a standard deviation of only 0.1% and maximum deviation of only 1%. The pressure control (PC) mode shows the best performance but cannot be used for growth experiment since the crystal growth increases the pressure in the channel with time. All the crystal growth experiments reported here are therefore performed using the flow control (FC) mode.

Calcite nucleation

At saturation index $\Sigma = 1.9$, nucleation occurs fast and some nuclei attach either to the PDMS or glass surfaces. Figure 6 A shows both a calcite and a vaterite nuclei present simultaneously in the middle of the channel. Since mixing occurs by diffusion, the highest concentration appears at the centre of the channel and the nuclei attach at the middle of the glass or PDMS surface allowing for good optical access and free space for subsequent growth. Changing the calcium carbonate concentration to 0.5 mM, the

vaterite is totally dissolved after 22 minutes and the calcite is left unchanged (Figure 6 B). The calcite nuclei are predominantly rhombohedral and the $10\bar{1}4$ surface attach to the glass or PDMS. The crystals can then grow freely on 5 of the 6 surfaces. Figure 6 C shows a vaterite nucleus that is chosen for growth in the channel and Figure 6 D shows the same crystal after 23 hours growth. This demonstrates how the microfluidic device can keep any polymorph stable for further study.

Calcite growth rate

We have performed very many growth rate experiments with the setup reported here. We repeatedly measured two limits to growth: Below $c = 0.5$ mM calcite crystals started dissolving, above this concentration they were growing and above $c = 0.8$ mM there was a risk of nucleation of new crystals in the device. Figure 7 shows the results of an experiment with fast change of solution concentration to obtain growth rates over the whole range of concentrations in practice available to this device. The experiment was performed with decreasing and then increasing concentrations in fast succession to check the "stability" of the growth (see results and discussion of growth rate dispersion / variability below). The growth rates, v, were determined from images from periods of 15 of the 25 minutes at each concentration. For the lowest growth rates of about 400 nm/h this means that the change in position of the crystal face was only 100 nm during 15 minutes. The error bars in Figure 7 are the standard deviations of the linear fits to the 60 positions recorded during the 15 minute period. These results show that the technique is fast and accurate.

Teng et al[16] summarized macroscopic growth rate laws as belonging to two types:

$$v = k' \left(e^{n\Sigma} - 1\right) \approx k' n \Sigma \approx k\Sigma, \text{ and } (4)$$

$$v = k_2 \left(e^{\Sigma} - 1\right)^n \approx k_2 \Sigma^n, \quad (5)$$

where the leading order approximations are valid when $\Sigma \ll 1$. Teng et al[16] found that the surface processes (growth only at screw dislocations) they observed and the rate they measured at $\Sigma < 1.5$ was consistent with equation (5) with $n = 2$. The growth rates we have measured are more consistent with equation (4) in the small range of concentration and saturation indices. The growth rate constants k and k_2 are a good basis for comparison with other data from the literature. The growth rate constants determined here and displayed in Figure 7 have a standard deviation of 5-9%.

The results in Figure 7 are for a crystal with two faces perpendicular and two faces parallel to the channel walls. The front face that receives fluid unperturbed by solid surfaces or crystal growth grows 30% faster than the two faces parallel to the fluid flow and 60% faster than the back surface facing downstream. This can be explained by the hydrodynamic conditions at the crystal surfaces. The fluid velocity, u, is zero at the surfaces and grows towards the middle of the channel. This results in a hydrodynamic boundary layer where only diffusion transports ions to the surface. The thickness, δ, of this boundary layer scales with the fluid velocity, u, and length of travel along the crystal surface, l, as $\delta \propto \sqrt{l/u}$. Calculating the boundary layer thickness on the back surface we find the ratio between the observed, diffusion limited growth rate, v_d, and the purely reaction limited growth rate, v_r, (see the Supplementary information) $v_d/v_r \sim 0.4$. This agrees well with the observed difference between the front and the back of crystal G of about 60%. Since the growth rates of the front surface are the closest we can come to pure reaction limited growth rate this is what we report in the table in Figure 7.

For most other crystals we have performed 5-20 hours growth experiments at the same concentration in the range 0.5-0.8 mM (see Table 1). In some cases the pressure increased during the experiment (due to crystal growth at the outlet) and we discard that part of the experiment since we could not measure the CO_2 concentration of the solution. In Table 1 we report the growth rate of the crystal surfaces growing fastest since they were facing the flow and less perturbed by the hydrodynamic boundary layer.

In Figure 8 we have plotted our measured

t	P	c_{CaCO_3}	Σ_p	v
mins	*mbar*		*mM*	*nm/h*
0-25	185	0.799±0.002	0.44	2320±34
25-50	182	0.750±0.002	0.37	1590±29
50-75	194	0.692±0.001	0.27	1091±40
75-100	189	0.658±0.002	0.21	981±59
100-125	206	0.593±0.002	0.09	701±38
125-150	189	0.560±0.002	0.02	651±44
150-175	205	0.593±0.002	0.09	676±33
175-200	190	0.640±0.002	0.18	894±48
200-225	199	0.692±0.002	0.27	1182±32
225-250	186	0.750±0.002	0.37	1458±29
250-275	193	0.801±0.002	0.44	1535±40

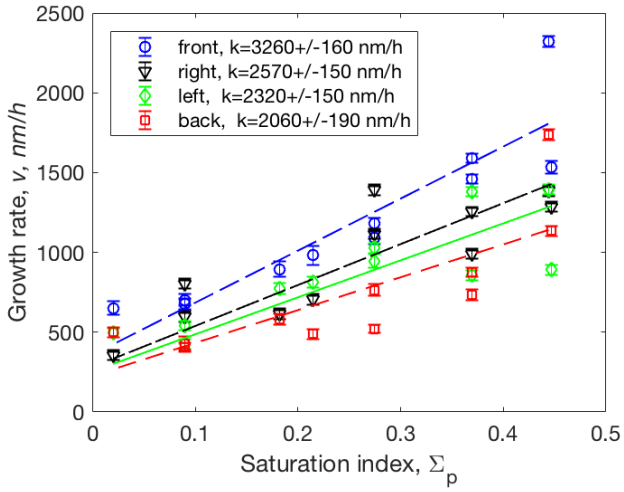

Figure 7: *Growth conditions and rates of crystal G. In less than 5 hours growth rates of four crystal faces were measured twice at 6 different $CaCO_3$ concentrations c_{CaCO_3}. Saturation indices Σ_p are calculated at $CaCO_3$ concentrations c and CO_2 partial pressures [mbar] $P_{CO_2} = 3.9 \cdot 10^{-4}(1013 + P)$, where P is the pressure (in this table) to drive the fluid flow. The growth rates in the table are those of the front face which is almost perpendicular to the fluid flow, the figure shows growth rates of all faces. The slopes of the fitted lines are the growth rate constants, k. The growth rate constant at the crystal surface facing the fluid flow is 60% higher than that of the surface at the back of the crystal due to the increasing effect of the diffusion boundary layer with distance of flow along the crystal.*

Table 1: *Growth conditions and growth rates of crystals A-F. Saturation indices Σ_p are calculated at $CaCO_3$ concentrations c_{CaCO_3} and CO_2 partial pressures [mbar] $P_{CO_2} = 3.9 \cdot 10^{-4}(1013 + P)$, where P is the pressure (in this table) to drive the fluid flow.*

Exp	P	c	Σ_p	v	δ_v
	mbar	*mM*		*nm/h*	*nm/h*
A	200	0.499	-0.11	8	10
B	400	0.706	0.24	1030	40
C	540	0.718	0.21	1020	60
D	250	0.79	0.41	1580	100
E	360	0.801	0.4	1600	100
F	200	0.801	0.45	1010	50

growth rates versus the calculated saturation indices (see also Figure 7). We have added 0.11 to the values Σ_p in Table 1 to account for the observed saturation concentration $c_{sat} = 0.5$ mM (at 25°C and $p = 200$ *mbar*) of our solutions. We have fit equation (4) to the growth rates in Table 1 and obtain the growth constant $k = 3260 \pm 160$ nm/h. At $\Sigma < 0.7$ we have used equation (4) to fit to calcite growth data measured by AFM,[9,16] $k_{AFM} = 20 \pm 5$ nm/h, and by batch crystallization,[11] $k_{Reddy} = 610 \pm 40$ nm/h. To our great surprise our growth rate constant is about 5 times higher than k_{Reddy} and about 160 times higher than k_{AFM}. If we use the growth rate equation (5) instead with a wider range of Σ, our growth rate constant k_2 is a factor 95 larger than that from Teng et al. We have checked and rechecked our lab notebooks and all our calculations several times. The experiments have been performed over a period of 3 years and in different physical versions of the same layout. The solutions have been prepared from scratch several times, the flow rates have been verified by many methods and calculations, the imaging length scale has been recalibrated and the imaging frame rate has been rechecked and verified.

Our first explanation for the two orders of magnitude difference was that the AFM experiments are much more affected by hydrodynamic boundary layers than our experiments. Traditional analysis of AFM flow cells indicate that this should not account for the large discrepancy: A typical AFM flow cell[52] has $l \sim 10^{-3}$ m and $u \sim 10^{-2}$ m/s. Since the flow is over a flat crystal surface $s_c/s \sim 1$. Although the boundary layer is 10 times thicker, the final reduction in observed growth rate in AFM experiments is then expected to be $v_d/v_r \sim 0.2$, only a factor 2 smaller than the back side of the crystals in our experiments. This means that in such a

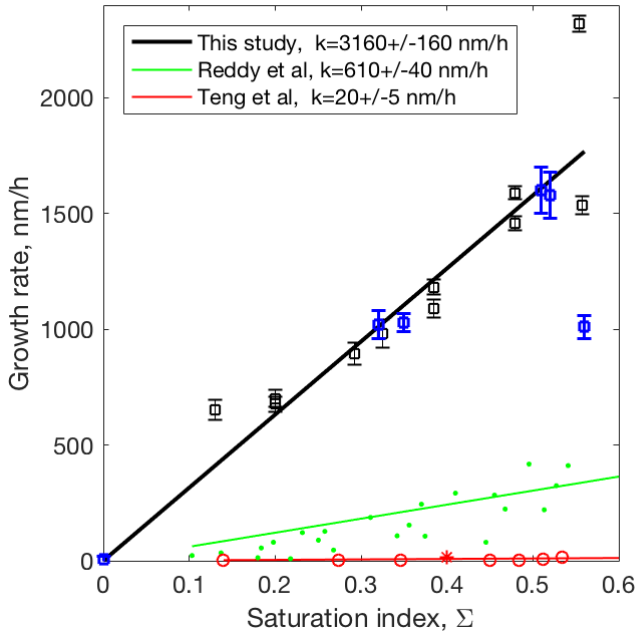

Figure 8: **Comparison of growth rate constants.** *Blue squares: v_{max} from Table 1, black squares: v from table in Figure 7, green dots: growth rates from Figure 3 of Reddy et al.,*[11] *red circles: growth rates from Table 2 of Teng et al.,*[16] *red asterisk: growth rate from Bracco et al.*[9] *The saturation index of our measurements have been corrected to be zero when there is no growth:* $\Sigma = \Sigma_p + 0.11$.

case we expect no more than a factor 2 difference between the growth rate on our front face and those in AFM measurements. However, a recent study by Peruffo et al[53] has critically analyzed the effect of dissolution/growth outside the region of interest (ROI) of the AFM measurement and the effect of spatially heterogeneous flow in AFM flow cells. They found that in the case of gypsum this could cause 1-2 orders of magnitude lower dissolution rates measured by AFM than by batch experiments.

Another difference between our measurements and AFM measurements is that our calcite crystals are untouched by human hands and have never experienced any other environment than the growth solution, whereas AFM experiments are typically performed on flat portions of cleaved Island spar crystals. It is conceivable that either contaminations in the crystal or strain energy due to the cleaving make these crystals less reactive than our newly nucleated calcite rhombs. Many practitioners do, however etch the cleaved calcite surface before starting growth in order to avoid this problem. It is possible that Island spar crystals that have grown very slowly over geological time have a very small dislocation density compared to our crystals. However, from a geometrical consideration, the fastest growth of a whole crystal will occur when the crystal face is covered by a single growth spiral around a dislocation core. If hydrodynamics and processes outside the ROI of the AFM cannot account for the discrepancy with our measurements then we must consider either rough step fronts instead of strait step trains or a much higher step density.

It is outside the scope of this paper to explain why growth rate constants for Island spar calcite crystals calculated from AFM measurements are 2 orders of magnitude smaller than we measure. Our measurements should, however prompt a serious discussion of what are actually the rate limiting mechanisms in different calcite growth rate experiments.

Conclusions

A novel method for studying nucleation and growth of $CaCO_3$ crystals in situ has been developed and tested rigorously. We demonstrate that precise flow control is essential and how this is achieved. The method has the advantage that one may study single crystals of polymorphs that are thermodynamically unstable in collections of many crystals and that one obtains precise and accurate growth rates without any extra assumptions. We also demonstrate that at low supersaturations where 2D nucleation does not occur we measure the growth rate constant of calcite to be 5 times larger than that reported by batch methods (that need additional measurement or assumption of reactive surface area) and two orders of magnitude larger than measured by AFM. Considering the large interest in calcite growth in for example geoscience, environmental science, and industry we consider that it is important to explain the discrepancy of growth rate constants between different methods. The method presented here can easily be applied to many other minerals.

Acknowledgement This project has received funding from the European Union's Horizon 2020 research and innovation programme under the Marie Sklodowska-Curie grant agreement no. 642976 (ITN NanoHeal) and from the Norwegian Research Council grant no. 222386.

Supporting Information Available

Additional information on experimental details and calculation of hydrodynamic boundary layers are available.

References

(1) Banner, J. L. Application of the trace element and isotope geochemistry of strontium to studies of carbonate diagenesis. *Sedimentology* **1995**, *42*, 805–824.

(2) Riding, R. Microbial carbonates: the geological record of calcified bacterial-algal mats and biofilms. *Sedimentology* **2000**, *47*, 179–214.

(3) Fairchild, I. J.; Treble, P. C. Trace elements in speleothems as recorders of environmental change. *Quaternary Science Reviews* **2009**, *28*, 449–468.

(4) Roehl, P. O.; Choquette, P. W. *Carbonate Petroleum Reservoirs*; 1985.

(5) Watabe, N. Crystal Growth of Calcium Carbonate in the Invertibrates. *Progress in crystal growth and characterization of materials* **1981**, *4*, 99–147.

(6) Colfen, H. Precipitation of carbonates: recent progress in controlled production of complex shapes. *Current opinion in colloid and interface science* **2003**, *8*, 23–31.

(7) Meldrum, F. C. Calcium carbonate in biomineralisation and biomimetic chemistry. *IInternational Materials Review* **2003**, *48*, 187–224.

(8) Carr, F. P.; Frederick, D. K. Calcium carbonate. 2000.

(9) Bracco, J. N.; Stack, A. G.; Steefel, C. I. Upscaling calcite growth rates from the mesoscale to the macroscale. *Environmental Science and Technology* **2013**, *47*, 7555–7562.

(10) Andersson, M. P.; Dobberschütz, S.; Sand, K. K.; Tobler, D. J.; De Yoreo, J. J.; Stipp, S. L. A Microkinetic Model of Calcite Step Growth. *Angewandte Chemie - International Edition* **2016**, *55*, 11086–11090.

(11) Reddy, M. M.; Plummer, L. N.; Busenberg, E. Crystal growth of calcite from calcium bicarbonate solutions at constant PCO2and 25C: a test of a calcite dissolution model. *Geochimica et Cosmochimica Acta* **1981**, *45*, 1281–1289.

(12) Hillner, P. E.; Manne, S.; Gratz, A. J.; Hansma, P. K. AFM images of dissolution and growth on a calcite crystal. *Ultramicroscopy* **1992**, *42-44*, 1387–1393.

(13) Stipp, S. L. S.; Eggleston, C. M.; Nielsen, B. S. Calcite Surface-Structure Observed at Microtopographic and Molecular Scales with Atomic-Force Microscopy (AFM). *Geochimica Et Cosmochimica Acta* **1994**, *58*, 3023–3033.

(14) Teng, H. H. Thermodynamics of calcite growth: baseline for understanding biomineral formation. *Science* **1998**, *282*, 724–727.

(15) Teng, H. H.; Dove, P. M.; Deyoreo, J. J. Reversed calcite morphologies induced by microscopic growth kinetics: Insight into biomineralization. *Geochimica et Cosmochimica Acta* **1999**, *63*, 2507–2512.

(16) Teng, H. H.; Dove, P. M.; De Yoreo, J. J. Kinetics of calcite growth: Surface processes and relationships to macroscopic rate laws. *Geochimica et Cosmochimica Acta* **2000**, *64*, 2255–2266.

(17) Ruiz-Agudo, E.; Putnis, C. V. Direct observations of mineral fluid reactions using atomic force microscopy: the specific example of calcite. *Mineralogical Magazine* **2012**, *76*, 227–253.

(18) Sand, K. K.; Tobler, D. J.; Dobberschütz, S.; Larsen, K. K.; Makovicky, E.; Andersson, M. P.; Wolthers, M.; Stipp, S. L. Calcite Growth Kinetics: Dependence on Saturation Index, Ca2+:CO32-Activity Ratio, and Surface Atomic Structure. *Crystal Growth and Design* **2016**, *16*, 3602–3612.

(19) Andreassen, J. P.; Hounslow, M. J. Growth and aggregation of vaterite in seeded-batch experiments. *AIChE Journal* **2004**, *50*, 2772–2782.

(20) Arvidson, R. S.; Ertan, I. E.; Amonette, J. E.; Luttge, A. Variation in calcite dissolution rates: A fundamental problem? *Geochimica et Cosmochimica Acta* **2003**, *67*, 1623–1634.

(21) Lüttge, A.; Arvidson, R. S.; Fischer, C. A stochastic treatment of crystal dissolution kinetics. *Elements* **2013**, *9*, 183–188.

(22) Colombani, J. The Alkaline Dissolution Rate of Calcite. *Journal of Physical Chemistry Letters* **2016**, *7*, 2376–2380.

(23) Neuville, A.; Renaud, L.; Luu, T. T.; Minde, M. W.; Jettestuen, E.; Vinningland, J. L.; Hiorth, A.; Dysthe, D. K. Xurography for microfluidics on a reactive solid. *Lab Chip* **2017**, *17*, 293.

(24) Pohl, A.; Weiss, I. M. Real-time monitoring of calcium carbonate and cationic peptide deposition on carboxylate-SAM using a microfluidic SAW biosensor. *Beilstein Journal of Nanotechnology* **2014**, *5*, 1823–1835.

(25) Chen, P.-C.; Wan, L.-S.; Xu, Z.-K. Bio-inspired CaCO3 coating for superhydrophilic hybrid membranes with high water permeability. *Journal of Materials Chemistry* **2012**, *22*, 22727.

(26) Liu, L.; Wu, F.; Ju, X. J.; Xie, R.; Wang, W.; Niu, C. H.; Chu, L. Y. Preparation of monodisperse calcium alginate microcapsules via internal gelation in microfluidic-generated double emulsions. *Journal of Colloid and Interface Science* **2013**, *404*, 85–90.

(27) Shi, X. W.; Tsao, C. Y.; Yang, X.; Liu, Y.; Dykstra, P.; Rubloff, G. W.; Ghodssi, R.; Bentley, W. E.; Payne, G. F. Electroaddressing of cell populations by co-deposition with calcium alginate hydrogels. *Advanced Functional Materials* **2009**, *19*, 2074–2080.

(28) Amici, E.; Tetradis-Meris, G.; de Torres, C. P.; Jousse, F. Alginate gelation in microfluidic channels. *Food Hydrocolloids* **2008**, *22*, 97–104.

(29) Tan, W. H.; Takeuchi, S. Monodisperse alginate hydrogel microbeads for cell encapsulation. *Advanced Materials* **2007**, *19*, 2696–2701.

(30) Huang, K.-S. Using a microfluidic chip and internal gelation reaction for monodisperse calcium alginate microparticles generation. *Frontiers in Bioscience* **2007**, *12*, 3061.

(31) Xu, B.-Y.; Yang, Z.-Q.; Xu, J.-J.; Xia, X.-H.; Chen, H.-Y. Liquidgas dual phase microfluidic system for biocompatible CaCO3 hollow nanoparticles generation and simultaneous molecule doping. *Chemical Communications* **2012**, *48*, 11635–11637.

(32) Zhang, C.; Dehoff, K.; Hess, N.; Oostrom, M.; Wietsma, T. W.; Valocchi, A. J.; Fouke, B. W.; Werth, C. J. Porescale study of transverse mixing induced CaCO3 precipitation and permeability reduction in a model subsurface sedimentary system. *Environmental Science and Technology* **2010**, *44*, 7833–7838.

(33) Boyd, V.; Yoon, H.; Zhang, C.; Oostrom, M.; Hess, N.; Fouke, B.; Valocchi, A. J.; Werth, C. J. Influence of Mg2+

on CaCO3 precipitation during subsurface reactive transport in a homogeneous silicon-etched pore network. *Geochimica et Cosmochimica Acta* **2014**, *135*, 321–335.

(34) Pibyl, M.; Šnita, D.; Marek, M. Nonlinear phenomena and qualitative evaluation of risk of clogging in a capillary microreactor under imposed electric field. *Chemical Engineering Journal* **2005**, *105*, 99–109.

(35) Song, W.; de Haas, T. W.; Fadaei, H.; Sinton, D. Chip-off-the-old-rock: the study of reservoir-relevant geological processes with real-rock micromodels. *Lab Chip* **2014**, *14*, 4382–4390.

(36) Wang, W.; Chang, S.; Gizzatov, A. Toward Reservoir-on-a-Chip: Fabricating Reservoir Micromodels by in Situ Growing Calcium Carbonate Nanocrystals in Microfluidic Channels. *ACS Applied Materials and Interfaces* **2017**, *9*, 29380–29386.

(37) Rodríguez-Ruiz, I.; Veesler, S.; Gómez-Morales, J.; Delgado-López, J. M.; Grauby, O.; Hammadi, Z.; Candoni, N.; García-Ruiz, J. M. Transient calcium carbonate hexahydrate (ikaite) nucleated and stabilized in confined nano- and picovolumes. *Crystal Growth and Design* **2014**, *14*, 792–802.

(38) Li, S.; Ihli, J.; Marchant, W. J.; Zeng, M.; Chen, L.; Wehbe, K.; Cinque, G.; Cespedes, O.; Kapur, N.; Meldrum, F. C. Synchrotron FTIR mapping of mineralization in a microfluidic device. *Lab Chip* **2017**, *17*, 1616–1624.

(39) Zeng, Y.; Cao, J.; Wang, Z.; Guo, J.; Lu, J. Formation of Amorphous Calcium Carbonate and Its Transformation Mechanism to Crystalline CaCO ₃ in Laminar Microfluidics. *Crystal Growth & Design* **2018**, *18*, 1710–1721.

(40) Yin, H.; Ji, B.; Dobson, P. S.; Mosbahi, K.; Glidle, A.; Gadegaard, N.; Freer, A.; Cooper, J. M.; Cusack, M. Screening of Biomineralization Using Microfluidics. *Analytical chemistry* **2009**, *81*, 473–478.

(41) Neira-Carrillo, A.; Pai, R. K.; Fernández, M. S.; Carreño, E.; Quitral, P. V.; Arias, J. L. Synthesis and characterization of sulfonated polymethylsiloxane polymer as template for crystal growth of CaCO3. *Colloid and Polymer Science* **2009**, *287*, 385–393.

(42) Neira-Carrillo, A.; Vásquez-Quitral, P.; Yazdani-Pedram, M.; Arias, J. L. Crystal growth of CaCO3induced by monomethylitaconate grafted polymethylsiloxane. *European Polymer Journal* **2010**, *46*, 1184–1193.

(43) Yin, H.; Ji, B.; Cusack, M.; Freer, A.; Dobson, P. S.; Gadegaard, N.; Jiang, J. Microfluidics in Biomineralization and Biomimicking Synthesis. uTAS2010. 2010; pp 986–988.

(44) Ji, B.; Cusack, M.; Freer, A.; Dobson, P. S.; Gadegaard, N.; Yin, H. Control of crystal polymorph in microfluidics using molluscan 28 kDa Ca2+-binding protein. *Integrative Biology* **2010**, *2*, 528.

(45) Yashina, A.; Meldrum, F.; Demello, A. Calcium carbonate polymorph control using droplet-based microfluidics. *Biomicrofluidics* **2012**, *6*, 22001–2200110.

(46) Seo, S. W.; Ko, K. Y.; Lee, C. S.; Kim, I. H. CaCO3 Biomineralization in Microfluidic Crystallizer. *Korean Chem. Eng. Res.* **2013**, *51*, 151–156.

(47) Gong, X.; Wang, Y. W.; Ihli, J.; Kim, Y. Y.; Li, S.; Walshaw, R.; Chen, L.; Meldrum, F. C. The Crystal Hotel: A Microfluidic Approach to Biomimetic Crystallization. *Advanced Materials* **2015**, *27*, 7395–7400.

(48) Beuvier, T.; Panduro, E. A. C.; Kwaśniewski, P.; Marre, S.; Lecoutre, C.; Garrabos, Y.; Aymonier, C.; Calvignac, B.; Gibaud, A. Implementation of

in situ SAXS/WAXS characterization into silicon/glass microreactors. *Lab Chip* **2015**, *15*, 2002–2008.

(49) Kim, Y.-Y.; Freeman, C. L.; Gong, X.; Levenstein, M. A.; Wang, Y.; Kulak, A.; Anduix-Canto, C.; Lee, P. A.; Li, S.; Chen, L.; Christenson, H. K.; Meldrum, F. C. The Effect of Additives on the Early Stages of Growth of Calcite Single Crystals. *Angewandte Chemie International Edition* **2017**, *200444*, 11885–11890.

(50) Ogino, T.; Suzuki, T.; Sawada, K. The formation and transformation mechanism of calcium carbonate in water. *Geochimica et Cosmochimica Acta* **1987**, *51*, 2757–2767.

(51) Charlton, S. R.; Parkhurst, D. L. Modules based on the geochemical model PHREEQC for use in scripting and programming languages. *Computers & Geosciences* **2011**, *37*, 1653–1663.

(52) Schmidt, W. U. Use of Atomic Force Microscopy to Image Surfaces during Fluid Flow. *Journal of The Electrochemical Society* **1994**, *141*, L85.

(53) Peruffo, M.; Mbogoro, M. M.; Adobes-Vidal, M.; Unwin, P. R. Importance of Mass Transport and Spatially Heterogeneous Flux Processes for in Situ Atomic Force Microscopy Measurements of Crystal Growth and Dissolution Kinetics. *Journal of Physical Chemistry C* **2016**, *120*, 12100–12112.

Graphical TOC Entry

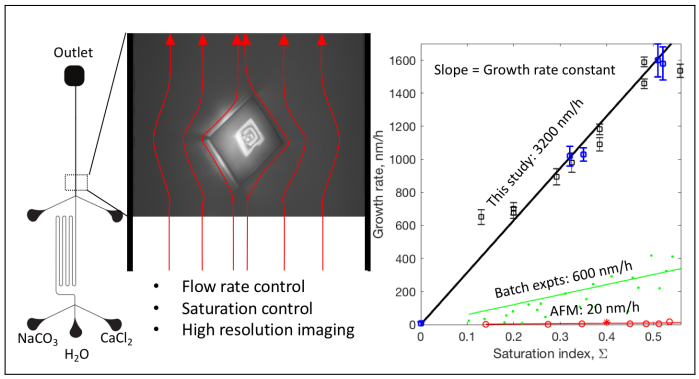

Calcite is important in Nature and industry. We present a new method for measuring calcite crystal growth rates from solution with precise control of flow, saturation and whole crystal size. We find that previous research using AFM to calculate calcite growth rate underestimate the growth rate constant by two orders of magnitude.

Microfluidic control of nucleation and growth of $CaCO_3$ - supplementary information

Lei Li, Jesus Rodriguez Sanchez, Felix Kohler, Anja Røyne, and Dag Kristian Dysthe*

Physics of Geological Processes (PGP), The NJORD Centre, Department of Physics, University of Oslo, POBox 1048 Blindern, 0316 Oslo

E-mail: d.k.dysthe@fys.uio.no
Phone: +47 90940996

Experimetal details

Figures 1 and 2 show the detailed setup for microfluidic flow control.

Diffusion and reaction control of growth rates

We follow Colombani[1] that analysed the effect of hydrodynamic boundary layers on calcite dissolution. Colombani uses the results of Jousse et al[2] for the hydrodynamic boundary layer thickness, δ:

$$\delta = 2.95 \left(\frac{\mu}{\rho}\right)^{1/6} D^{1/3} \sqrt{l/u}, \qquad (1)$$

where μ is the viscosity, ρ the density, D the diffusion coefficient, u the far field velocity and l is the length along the crystal surface.

For pure reaction control of crystal growth the fluid concentration at the crystal surface, c_s, equals the imposed concentration, c, far from the surface, $c_s = c$ and the reaction controlled growth rate is

$$v_r = k_c(c/c_{sat} - 1), \qquad (2)$$

where c_{sat} is the saturation concentration and k_c the growth rate constant with dimension $[k_c]$=m/s ($k_c' = k_c\bar{V}$ where $[k_c']$=mol/m^2/s and $\bar{V}$ is the molar volume of calcite). We now calculate the growth rate, v_d, limited by diffusion through a hydrodynamic boundary layer. The balance of diffusion flux and growth flux (see Equation 1 in[1]) yields an expression for the diffusion limited growth rate:

$$v_d = \frac{sD(c_s - c)\bar{V}}{s_c\delta} = k_c(c_s/c_{sat} - 1), \qquad (3)$$

where c_s is the concentration at the crystal surface, s_c is the area of the crystal, s is the area of the hydrodynamic boundary layer (see Figure 1 in[1]) and D is the diffusion coefficient. From this one finds the concentration at the crystal surface:

$$c_s = \frac{\gamma c_{sat} + c}{1 + \gamma}, \quad \gamma = \frac{k_c\delta s}{Dc_{sat}s_c\bar{V}} \qquad (4)$$

and the ratio between the measured, diffusion limited and the purely reaction limited growth rates is

$$\frac{v_d}{v_r} = \frac{c_s/c_{sat} - 1}{c/c_{sat} - 1} = \frac{1}{1 + \gamma}. \qquad (5)$$

We may evaluate this for our experiments with a crystal of about l ∼10 μm, $u \sim 10^{-2}$ m/s, $\mu/\rho \sim 10^{-6}$ m^2/s, $D = 10^{-9}$ m^2/s to get a boundary layer of δ=9 μm. Since $\delta \sim l$ the ratio of the boundary layer surface to the crystal surface is $s/s_c \sim 4$ and $k_c = 2700$ nm/h $= 7.5 \cdot 10^{-9}$ m/s, then $\gamma \sim 1.5$ and $v_d/v_r \sim 0.4$.

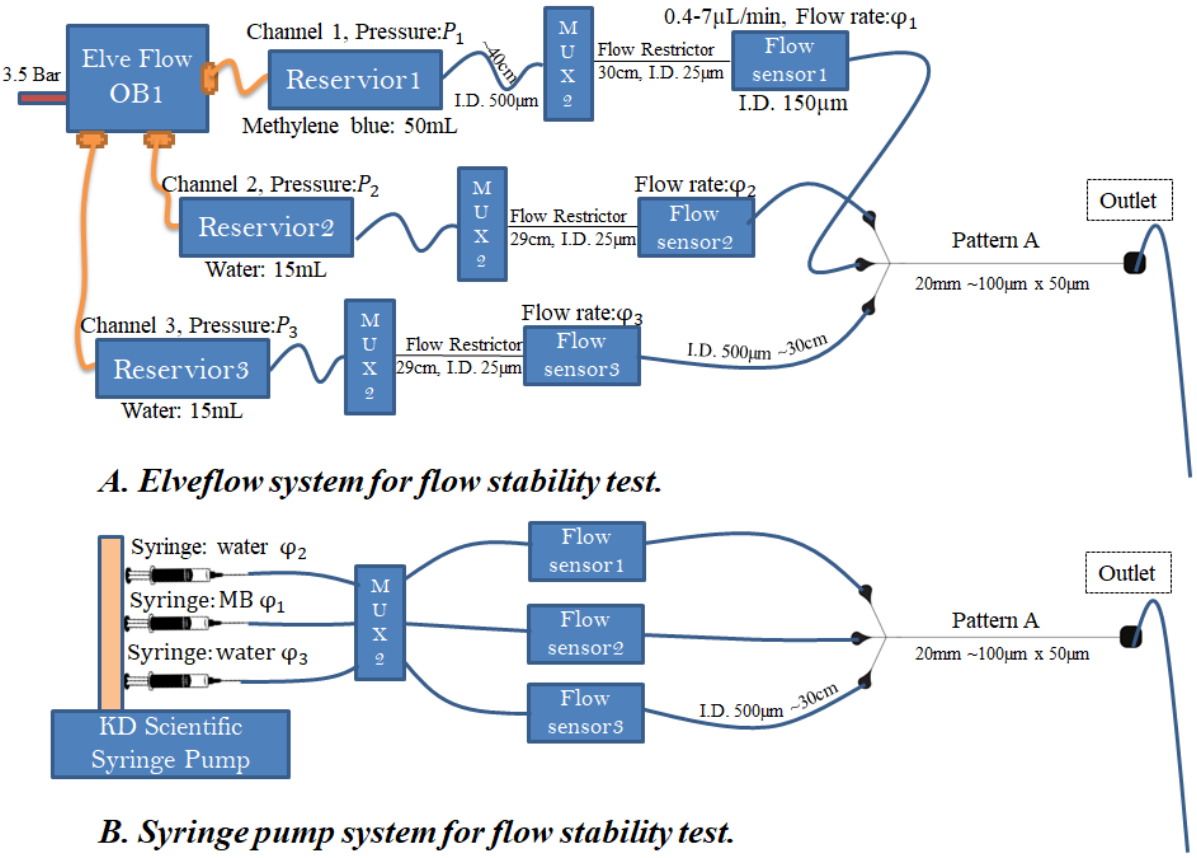

Figure 1: Detailed diagram of flow rate control system and microfluidic chip for flow stability tests.

References

(1) Colombani, J. Measurement of the pure dissolution rate constant of a mineral in water. *Geochimica et Cosmochimica Acta* **2008**, *72*, 5634–5640.

(2) Jousse, F.; Jongen, T.; Agterof, W. A method to dynamically estimate the diffusion boundary layer from local velocity conditions in laminar flows. *International Journal of Heat and Mass Transfer* **2005**, *48*, 1563–1571.

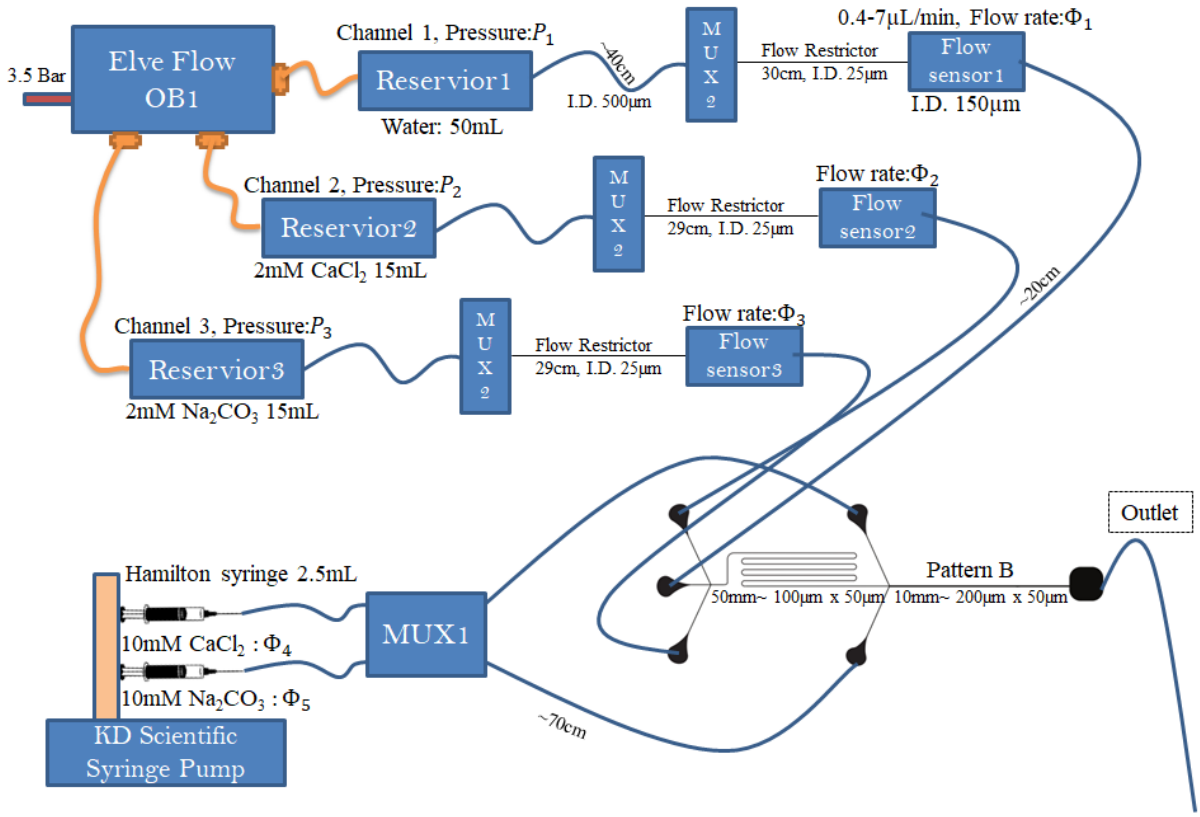

Figure 2: Detailed diagram of flow rate control system and microfluidic chip for nucleation and growth experiments.